*International Journal of Thermophysics, Vol. 21, No. 4, 2000*

# Numerical Analysis of a Radiant Heat Flux Calibration System

**S. Jiang,[1] T. J. Horn,[2] and V. K. Dhir,[1,3]**

*Received October 8, 1999*

Heat flux gauges are one of the devices that are used to determine the heat loads to which high-speed aerospace structures are subjected during flight. Prior to installation, these gauges are calibrated. The calibration system must be well understood if the heat flux gauges are to provide useful data during flight tests. A pseudo three-dimensional model of the radiant heat flux gauge calibration system was developed. The radiant heat flux gauge calibration system consists of a graphite plate heater and a circular foil heat flux gauge. The numerical model simulates the combined convection, radiation, and mass loss by chemical reaction on the graphite plate surface. It can be used to identify errors due to heater element erosion, and the deviations in the predicted heat fluxes due to uncertainties in various physical parameters of the system. A fourth-order finite difference scheme is used to solve the steady-state governing equations and to determine the temperature distribution in the gauge and the graphite plate, the incident heat flux on the gauge face, and the flat plate erosion. Initial gauge heat flux predictions from the model are found to be within $\pm 5\%$ of experimental results.

**KEY WORDS:** calibration; copper substrate; foil gauge; graphite plate; heat flux gauge.

## 1. INTRODUCTION

Uncertainties in radiant heat flux gauge calibrations are typically assumed to be of the order of $\pm 10\%$. The National Institute of Standards and Technology (NIST) is currently working to reduce this uncertainty

[1] Department of Mechanical and Aerospace Engineering, University of California Los Angeles, Los Angeles, California 90095, U.S.A.

[2] National Aeronautics and Space Administration, Dryden Flight Research Center, Edwards, California 93523, U.S.A.

[3] To whom correspondence should be addressed.



0195-928X/00/0700-0941$18.00/0 

significantly at heat flux levels up to $200\,\mathrm{kW \cdot m^{-2}}$ as described by Holmberg et al. [1], Grosshandler and Blackburn [2], and Murthy and Tsai [3]. However, aerodynamic heating in hypersonic flight can generate heat flux levels well in excess of this level. The Flight Loads Laboratory (FLL) at NASA's Dryden Flight Research Center performs radiant thermal-structural tests on aerospace vehicle structures which represent aerodynamic heat fluxes up to $1100\,\mathrm{kW \cdot m^{-2}}$. This paper describes a numerical analysis which was undertaken in the FLL to reduce radiant heat flux calibration uncertainties at heat fluxes up to $1100\,\mathrm{kW \cdot m^{-2}}$.

The radiant heat flux gauge calibration system described in this work uses an electrically heated graphite plate as a heat source. (A detailed description is given by Horn [4].) The main objective of the work described here is to model numerically the flat plate heater and to compare numerical and experimental results in an effort to quantify and, if possible, reduce errors in the calibration system. A pseudo-three-dimensional model of the system was developed. The graphite plate is modeled in three dimensions but under the assumption of axisymmetry; the conduction equation in the heat flux gauge is solved in two dimensions. The results have been compared with data from experiments. The numerical model provides the temperature distribution in the graphite plate and the copper support structure as well as the heat flux at the gauge foil surface. The finite difference scheme was used in the numerical model. The boundary conditions on the front face of the heat flux gauge include heat received by radiation from the graphite plate and lost to the ambient atmosphere by natural convection. Heat transfer by forced convection of water is modeled on the back face of the copper support structure. Heat is transferred from the graphite plate by natural convection and radiation to the ambient surroundings as well as to the heat flux gauge on one side of the plate. In addition, oxidation of the graphite plate, which impacts the power input, is included in the model.

## 2. EXPERIMENT

The heat flux gauge calibration system studied in this work consists of a graphite plate clamped between two copper electrodes (see Fig. 1). The graphite plate undergoes ohmic heating as a high current (up to 2400 A), at a low voltage ($<24$ V), is passed through the plate. The plate can reach temperatures up to 2800°C. Calibrations can be transferred from one heat flux gauge to another by placing one heat flux gauge on each side of the graphite plate, as shown in Fig. 2.

The system is operated in air, which results in oxidation of the graphite plate. However, graphite remains the material of choice for the flat plate heater because it maintains its strength throughout its operating temperature

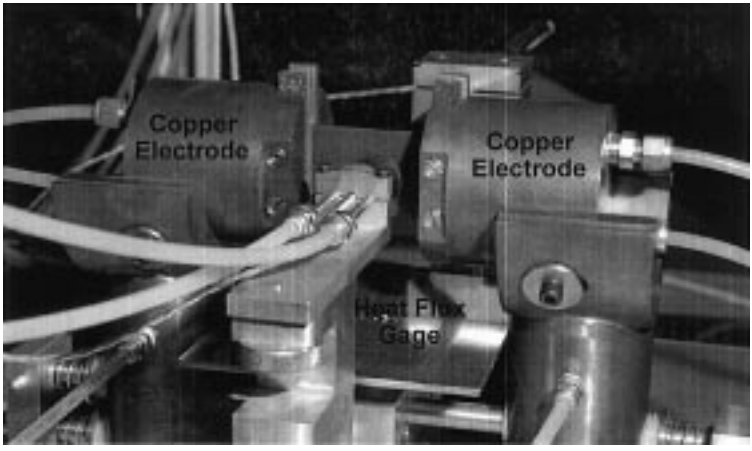


**Fig. 1.** Heat flux calibration system, side view.

range. Manufacturing the plate from a high-temperature metal such as molybdenum, tantalum, or tungsten, is not practical since these materials could sag and are subject to severe oxidation at the peak plate operating temperatures. Coating of either the graphite plate or a metallic substitute is not feasible since nonoxidizing metals, such as gold, melt well below 2800°C and ceramic coatings would inevitably have some cracks, which would allow oxidation to occur. Installing the flat plate heater in a vacuum chamber or inert gas environment is not practical due to the short duration of the calibration test and the resulting need to change test sensors frequently.

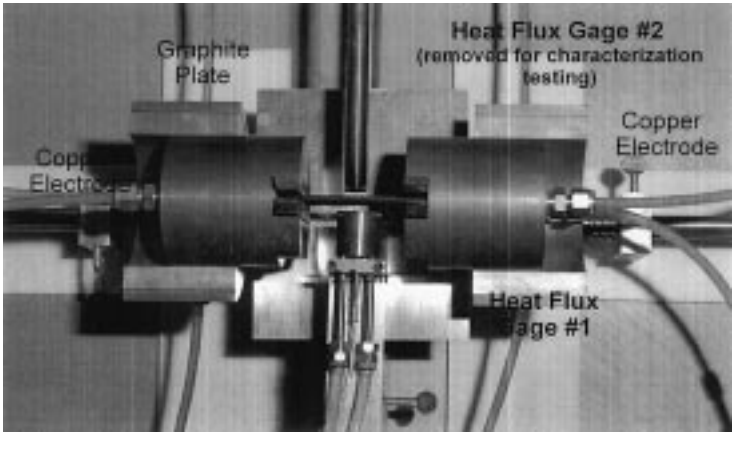


**Fig. 2.** Heat flux calibration system, top view.

The experiments performed to support the characterization of the flat plate heater utilized a circular foil heat flux gauge to measure the heat flux. The calibration supplied by the gauge manufacturer was used for comparison purposes. The second heat flux gauge was eliminated. Other measurements include the surface temperature, voltage across the plate, current through the plate, and plate erosion.

An infrared pyrometer, described by Cameron [5], measured the plate surface temperature at the center of the unobstructed side of the plate (Fig. 3). The target spot size was approximately 1 cm in diameter. The pyrometer uses a laser-based technique to measure emissivity and compute the temperature corrected for emissivity. It also incorporates through-the-lens sighting to aid in aiming and focusing the pyrometer optics on the measurement location. A wire-mesh grid placed over the flat graphite plate provided features on which to aim and focus. The grid was removed prior to testing.

Voltage was measured at the copper electrodes. Electric current passing through the graphite plate was also measured. The voltage, current, and heat flux data were recorded on a personal computer-based data acquisition system using voltmeters, a GPIB interface, and associated data acquisition software. Temperature data were logged every 10 s on board the infrared pyrometer and printed out after each test. Plate thickness was measured at the center of the plate using a micrometer before and after each test. Erosion of the top and bottom of the plates was measured posttest using a taper gauge and flat surface.

Tests were performed at nominal heat fluxes of 100, 200, 350, and 450 $kW \cdot m^{-2}$. Tests were run for 2, 4, 6, 8, and 10 min for each nominal heat flux. This matrix allowed the acquisition of voltage, current, and plate

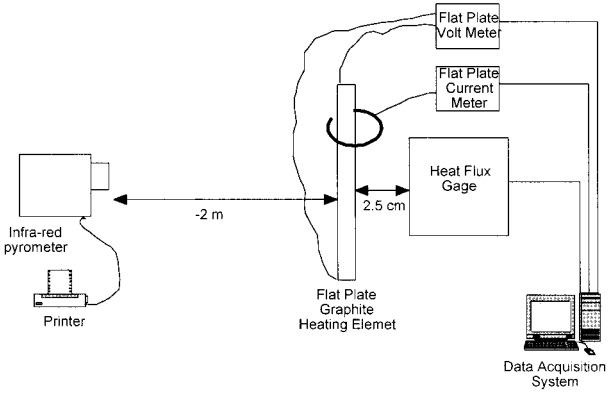


**Fig. 3.** Schematic of the test system.

erosion data as a function of heat flux (i.e., plate temperature) and run time. The experimental data presented in this paper were obtained during the nominal 450 $kW \cdot m^{-2}$, 10-min run.

A typical test proceeded as follows.

1. Measure the thickness of a new graphite plate.
2. Install the plate between the copper electrodes. The four set screws shown in Fig. 1 secure the plate and are uniformly torqued using a torque limiting screwdriver.
3. Apply minimum power to the flat plate and visually check for uniform heating as the plate begins to glow.
4. Remove power from plate. Retorque set screws and recheck plate heating or proceed to next step as required.
5. Start data acquisition and recording.
6. Apply power to the plate by setting the manual power supply control to the predetermined level which corresponds to the desired nominal heat flux.
7. Continue power application for the desired length of time without readjusting the manual power supply control.
8. Remove power from the plate when desired run time has been reached.
9. Remove graphite plate from between the electrodes.
10. Measure the eroded plate thickness as well as the top and bottom erosion.

Some additional remarks are necessary regarding Steps 3, 6, and 7 above. Some small amount of erosion occurs when the plate is checked for uniform heating (Step 3 above). The minimum power possible is used for this run, and the total time during which the plate is energized is less than 1 min. The erosion caused in Step 3 is extremely small and cannot be measured without disturbing the test setup, which would introduce still more errors into the heat flux measurement.

The nominal heat flux values mentioned earlier are only target values. The resolution of the manual power supply control allows the target heat flux to be set within 30 $kW \cdot m^{-2}$ in Step 6. For this reason, the heat flux data presented in this report will differ slightly from the nominal, or target, value.

Step 7, above, indicates that the manual power supply control is not adjusted once it is set for the desired heat flux. The constant power supply

setting and plate erosion result in a significant decrease in the measured heat flux (up to 20%) and flat plate current (up to 32%) while causing a voltage increase of up to 5%.

## 3. NUMERICAL MODELING

A schematic diagram of the experimental setup is shown in Fig. 4. The numerical model developed in this study includes conduction heat transfer within the graphite plate and the heat flux gauge and heat generation within the graphite plate and convective, radiative, and mass transfer boundary conditions. The mathematical model was based on the three-dimensional (3-D) geometry of the graphite plate and a 2-D axisymmetric model for the heat flux gauge. Analysis was also carried out using a 2-D model of the graphite plate and the copper structure. In this case, only a cross section of the graphite plate and the copper substrate obtained by passing a vertical plane through the graphite plate and the copper substrate midway between the electrodes was used. Figure 5 shows the configuration that was used to carry out the 2-D analysis. However, all of the results reported in this work are for a 3-D model.

The process is assumed to be quasi-steady state, i.e., heat conduction within the graphite plate and heat flux gauge is essentially steady state at any given moment in time even though the boundary conditions (current through the plate, mass loss, etc.) vary slowly with time. This assumption is implemented in the numerical model by using an implicit finite difference method to solve the steady-state heat conduction equations at discrete time steps (1-s intervals). The mass loss from the graphite plate over 1 s is computed after each time step. The next time step conduction solution proceeds

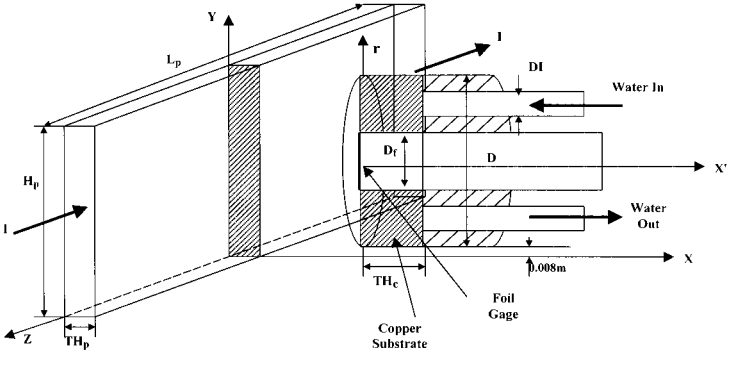


**Fig. 4.** Schematic of the graphite plate and heat flux gauge with the computational cross section.

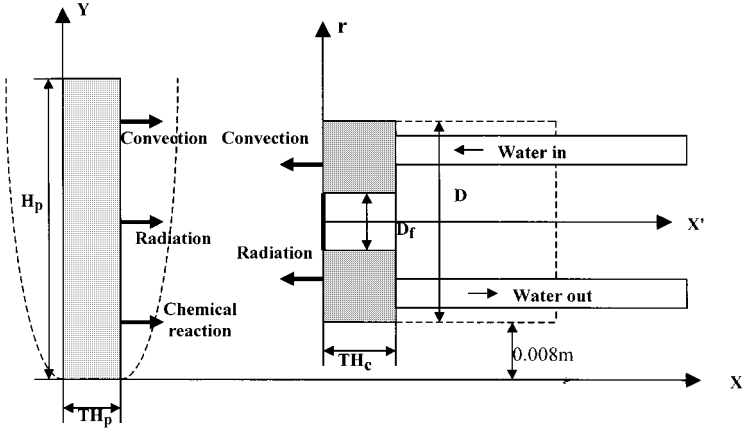


**Fig. 5.** Computational regime.

with a new plate shape, as determined from the previous mass loss calculation, and a new current through the flat plate, as measured during the experiment.

### 3.1. Numerical Model for the Graphite Plate

As shown in Fig. 4, the length of the plate is $L_p$, the height is $H_p$, and the thickness is $TH_p$. The steady-state governing energy equation for the graphite plate is

$$\frac{\partial}{\partial x}\left(k_p \frac{\partial T}{\partial x}\right)+\frac{\partial}{\partial y}\left(k_p \frac{\partial T}{\partial y}\right)+\frac{\partial}{\partial z}\left(k_p \frac{\partial T}{\partial z}\right)+Q'''=0 \tag{1}$$

where $k_p$ is the graphite plate thermal conductivity. Information provided by the graphite manufacturer indicates that the type ATJ graphite used in the plate is relatively isotropic. Therefore, the value used for $k_p$ is the same in all directions. The thermal conductivity of graphite steadily decreases from room temperature (25°C) to 3500°C. The functional dependence is provided by the graphite plate manufacturer. The temperature dependence used in the numerical calculation is interpolated from the curve supplied by the manufacturer. The graphite plate is heated by passing electric current through it. The model incorporates this as a heat generation term, $Q'''$, as

$$Q''' = \frac{I^2 R}{L_p H_p TH_p} \left(\mathrm{W \cdot m^{-3}}\right) \tag{2}$$

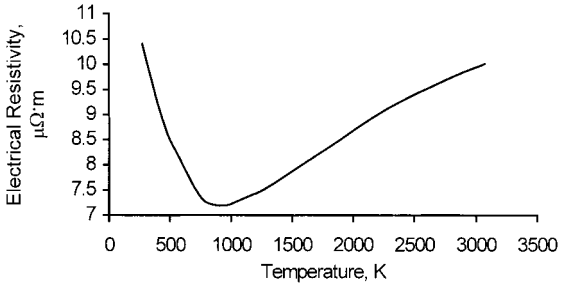


**Fig. 6.** ATJ graphite electrical resistivity vs temperature.

where $I$ is the electrical current and $R$ is the electrical resistance in the direction of current flow. The resistance $R$ is calculated as

$$R = \frac{\lambda L_p}{H_p T H_p} \tag{3}$$

where $\lambda$ is the specific resistance. It is also a function of temperature. As shown in Fig. 6, the specific resistance decreases from room temperature at 298 K until about 773 K, and thereafter, it increases. At the final experimental temperature of 2110 K, it has almost the same value as that at room temperature. The temperature dependence employed in the numerical calculations is interpolated from the curve provided by the manufacturer and shown in Fig. 6. Since $\lambda$ varies with temperature, the heat generation rate in the graphite plate varies with the position of each computational node.

The boundary conditions employed in the model are

$$x = 0; \qquad -k_p \frac{\partial T}{\partial x} = \sigma \varepsilon_p (T^4 - T_e^4) + h_{cv}(T - T_e) - \dot{m}''_v \, \Delta H_c \tag{4}$$

$$x = TH_p; \qquad -k_p \frac{\partial T}{\partial x} = q_p + h_{cv}(T - T_e) - \dot{m}''_v \, \Delta H_c \tag{5}$$

$$y = 0; \qquad -k_p \frac{\partial T}{\partial y} = h^d_{ch}(T - T_e) + \sigma \varepsilon_p (T^4 - T_e^4) - \dot{m}''^{\,d}_h \, \Delta H_c \tag{6}$$

$$y = H_p; \qquad -k_p \frac{\partial T}{\partial y} = h''_{ch}(T - T_e) + \sigma \varepsilon_p (T^4 - T_e^4) - \dot{m}''^{\,u}_h \, \Delta H_c \tag{7}$$

$$z = 0; \qquad -k_p \frac{\partial T}{\partial z} = 0 \tag{8}$$

$$z = L_p/2; \qquad -k_p \frac{\partial T}{\partial z} = \sigma \varepsilon_p (T^4 - T_e^4) + h_{cv}(T - T_e) - \dot{m}''_v \, \Delta H_c \tag{9}$$

At $x = 0$, heat is lost by radiation and convection to the ambient surroundings and gained because of the chemical reaction. At $x = TH_p$, the boundary conditions include radiation, chemical reaction, and convection to the ambient surroundings as well as radiant exchange with the heat flux gauge face. At $y = 0$, $y = H_p$, and $z = L_p/2$, heat is lost by radiation and natural convection and is generated by combustion. Equations (6), (7), and (9) represent this balance. In Eq. (5), $q_p$ is the net radiation heat transfer from the graphite plate surface. It includes the radiation heat flux from the graphite plate to ambient and to the heat flux gauge, which consists of copper substrate and foil gauge, minus the radiation from them that is absorbed by the graphite plate. The heat flux is obtained as

$$q_p = \sigma\varepsilon_p T_p^4 - F_{p\to c}\sigma\varepsilon_c T_c^4\varepsilon_p - F_{p\to f}\sigma\varepsilon_f T_f^4\varepsilon_p - F_{p\to e}\sigma\varepsilon_e T_e^4\varepsilon_p \tag{10}$$

where $F_{p\to c}$ and $F_{p\to f}$ are the shape factors from the graphite plate to the copper substrate and the foil gauge, respectively. These shape factors change with the geometry of the graphite plate and the distance between the graphite plate and the gauge. In carrying out the numerical calculations, the shape factor for a particular node is calculated by summing the contributions from all the other nodes.

In Eqs. (6) and (7), $h_{ch}$ is the average natural convection coefficient for a horizontal surface as given in standard textbooks (e.g., Ref. 6):

$$h_{ch} = h_{ch}^0 \frac{B_h}{\exp B_h - 1} \tag{11}$$

where the blowing parameter $B_h$ for heat transfer is defined as

$$B_h = \frac{n_{1,s} Cp_1 + n_{2,s} Cp_2}{h_c^0} \tag{12}$$

The blowing parameter is included to account for evolution of $CO_2$ with oxidation of graphite.

In Eq. (11), the heat transfer coefficient for zero mass transfer, $h_{ch}^0$, for the upper surface is obtained as

$$h_{ch}^{0,u} = \frac{0.54(Gr\ \mathrm{Pr})^{1/4} k_p}{D_{hp}} \tag{13}$$

and that for the downward facing surface as

$$h_{ch}^{0,d} = \frac{0.82(Gr\ \mathrm{Pr})^{1/5} k_p}{D_{hp}} \tag{14}$$

where $D_{hp}$ is the hydraulic diameter of the surface.

In Eqs. (4), (5), and (9), $h_{cv}$ is the average natural convection heat transfer coefficient for a vertical plate surface and is given by

$$h_{cv} = h^0_{cv} \frac{B_h}{\exp B_h - 1} \tag{15}$$

The heat transfer coefficient for zero mass transfer is

$$h^0_{cv} = \frac{0.68 + 0.67(Gr\ \mathrm{Pr}\ \varphi)^{1/4} k_p}{D_{hp}} \tag{16}$$

For the experimental conditions, at steady state ($T \sim 2000$ K), $Gr$ is less than $10^9$, and, as such, a laminar boundary layer forms on the graphite plate surface. The Prandtl number function, $\varphi$, is defined as

$$\varphi = \left[ 1 + \left( \frac{0.492}{\mathrm{Pr}} \right)^{9/16} \right]^{-16/9} \tag{17}$$

As a result of chemical reaction of carbon with oxygen to form $CO_2$, $3.28 \times 10^7$ J of heat is released per kg of carbon. The mass transfer rate $\dot{m}''$ is

$$\dot{m}'' = \eta^0 \frac{\ln(1 + \beta_{1m})}{\beta_{1m}} \beta_{1m} \tag{18}$$

where $\ln(1 + \beta_{1m})/\beta_{1m}$ is the mass transfer blowing factor and $\beta_{1m}$ is the mass driving force as given by Mills [6]. It is obtained as

$$\beta_{1m} = \frac{m_{1,e} - m_{1,s}}{m_{1,s} - n_{1,s}/\dot{m}''} \tag{19}$$

In Eq. (19), $m_{1,s}$ is the species 1 mass concentration on the surface of the graphite plate, denoting 1 as oxygen. Since the chemical kinetics is so rapid, the reaction is diffusion controlled. The gas mixture at the graphite plate surface is in equilibrium with the solid carbon. The equilibrium data indicate that the concentration of oxygen at the surface is essentially zero, i.e., $m_{1,s} = 0$. In Eq. (19), $m_{1,e}$ is the species concentration in ambient air. It is equal to 0.231. The ratio between the oxygen mass flux transferred to the graphite plate surface and the total mass transfer rate is $n_{1,s}/\dot{m}''$.

By using the analogy between heat and mass transfer, the zero-mass transfer-limit mass transfer conductance, $\eta^0$, for mass transfer is obtained by replacing the Prandtl number by the Schmidt number and $k_p$ by $\rho D_{12}$ in Eqs. (13), (14), and (16), with $D_{12}$ as the binary diffusion coefficient.

### 3.2. Numerical Model for the Heat Flux Gauge Consisting of a Copper Substrate and a Foil Gauge

The foil gauge is made of a piece of constantan foil held in the copper substrate of diameter $D$ and thickness $TH_c$ as shown in Fig. 4. The foil receives heat by radiation from the graphite plate and loses heat by radiation and conduction to the surrounding copper substrate. The copper block receives heat by radiation from both the graphite plate and the constantan foil. But the contribution from the foil is much smaller than that from the graphite plate. Thermocouples are placed in the center of the foil and the junction between the foil and the copper substrate. The calibration constant relates the heat flux to the output of the thermocouple in millivolts.

#### *3.2.1. Numerical Model for the Copper Substrate*

Boundary conditions on the front face are radiation heat transfer and natural convection in air. Forced convection of water boundary condition is imposed on the back face. Radiation exchange with the foil gauge occurs in the center. Assuming axisymmetry, the governing energy equation for the copper substrate is

$$\frac{1}{r}\frac{\partial}{\partial r}\left(r\frac{\partial T_c}{\partial r}\right)+\frac{\partial^2 T_c}{\partial x'^2}=0 \tag{20}$$

The boundary conditions are

$$r=D_f/2; \qquad -k_c\frac{\partial T_c}{\partial r}=q_{c\to f}\approx 0 \tag{21}$$

$$r=D/2; \qquad -k_c\frac{\partial T_c}{\partial r}=h_{cD}(T_c-T_e) \tag{22}$$

$$x'=0; \qquad -k_c\frac{\partial T_c}{\partial x'}=-q_c+h_{cv}(T_c-T_e) \tag{23}$$

$$x'=TH_c; \qquad -k_c\frac{\partial T_c}{\partial x'}=h_{water}(T_c-T_{water}) \tag{24}$$

where $h_{cD}$ is the heat transfer coefficient for the cylindrical surface. It is obtained from Eq. (25)

$$h_{cD}=\left[0.36+\frac{0.518(Gr_D\,\mathrm{Pr})^{1/4}}{[1+(0.559/\mathrm{Pr})^{9/16}]^{4/9}}\right]\frac{k_c}{D} \tag{25}$$

In a manner similar to $q_p$, $q_c$ is the net radiation heat transfer into the copper surface. It includes three parts: the net radiation heat flux from the graphite plate and ambient and heat loss to the surroundings.

$$q_c = F_{c\to p}\sigma\varepsilon_p T_p^4\varepsilon_c + F_{c\to e}\sigma\varepsilon_e T_e^4\varepsilon_c - \sigma\varepsilon_c T_c^4 \tag{26}$$

The net radiation exchange with the back face of the foil gauge can be obtained as

$$q_{c\to f} = \sigma\varepsilon_c T_c^4 - F_{c\to f}\sigma\varepsilon_f T_f^4\varepsilon_c \tag{27}$$

Forced convection cooling occurs due to water flow over the back face of the copper substrate. Water enters tube 1 on one side of the gauge structure, circles around the channel inside the gauge structure, and then exits from the tube on the other side. The inlet water temperature is 25°C. The water velocity $V$ is $\sim 1\ \mathrm{m\cdot s^{-1}}$. The Reynolds number corresponding to this velocity is approximately $9\times 10^4$. Thus, the turbulent flow heat transfer coefficient, $h_{water}$, is obtained as

$$h_{water} = \frac{0.023\ \mathrm{Re}^{0.8}\ \mathrm{Pr}^{0.4}\ k_{water}}{DI} \tag{28}$$

where $DI$ is the inside diameter of the channel as shown in Fig. 4.

### 3.2.2. *Numerical Model for the Foil Gauge*

The foil is made of a very thin sheet of constantan. It receives radiation from the graphite plate and loses heat by radiation and conduction to the copper substrate. The thickness, $\delta$, of the foil gauge depends on the type of thermal gauge. The foil in the heat flux gauge used in the experiments was 51 $\mu$m thick. With a foil diameter of 4 mm, the ratio of the diameter to the thickness is 80:1. Therefore, only one-dimensional radial conduction in the foil is considered. The governing equation is

$$-k_f\frac{\partial^2 T_f}{\partial r^2} = (q_{f\to p} - q_{f\to c})/\delta \tag{29}$$

where $q_{f\to p}$ is the net radiative heat flux from the graphite plate and $q_{f\to c}$ is the radiation to the copper substrate. These heat fluxes are expressed as

$$q_{f\to c} = \sigma\varepsilon_f T_f^4 - F_{f\to c}\sigma\varepsilon_c T_c^4\varepsilon_f \tag{30}$$

$$q_{f\to p} = \sigma\varepsilon_f T_f^4 - F_{f\to p}\sigma\varepsilon_p T_p^4\varepsilon_f \tag{31}$$

The boundary conditions are adiabatic in the foil center and isothermal at the edge:

$$r = 0; \qquad \frac{\partial T}{\partial r} = 0 \tag{32}$$

$$r = D_f/2; \qquad T = T_c \tag{33}$$

### 3.3. Calculation Procedure

During the heating of the graphite plate, chemical reaction involves burning of carbon in air. The reaction is $C + O_2 = CO_2$. Since carbon is continuously consumed at the plate surface, the shape of the graphite plate changes with time. Yet the plate temperature does not change rapidly, and the change is small. As such, at each erosion time step (1 s), the temperature is quasi-steady. In carrying out the numerical calculations, at each erosion time step, the following steps were used.

1. Give the initial temperature of the graphite plate and the heat flux gauge.
2. Numerically solve the governing equation with the appropriate boundary condition and obtain a new temperature distribution.
3. Use the graphite plate new temperature distribution in the radiation boundary condition for the heat flux gauge, update the temperature of the heat flux gauge, and use it for the radiation boundary condition of the graphite plate.
4. Repeat Step 2 onward until the temperatures converge to a unique value.
5. From the erosion rate of the graphite plate, calculate the shape change due to combustion and, thereafter, obtain the new value of the resistance and the new shape factor between the graphite plate and the heat flux gauge. The values are used for the next time step.
6. Repeat from Step 2 to Step 5 until the final time of the experiment.

## 4. RESULTS AND DISCUSSION

Comparison is made between the experimental data and the numerical calculations. Discussion of the results will include the temperature distribution, graphite plate erosion, heat flux calibration, grid sensitivity, and possible reasons for differences between the experimental data and the numerical calculations.

### 4.1. Temperature Distribution

The comparison of the 2-D and 3-D cases for temperature contours in the midplane of both graphite plate and copper substrate containing the foil gauge are shown in Figs. 7 and 8. It can be observed that the temperature difference between the two cases is only a few degrees. As a result, the 2-D assumption is not found to be unrealistic. However, all results reported in this work were obtained with the pseudo three-dimensional model.

The temperature contours shown in Figs. 7 and 8 were computed for the beginning of the experiment when little erosion of graphite plate had taken place. The measured surface temperature at the vertical center of the graphite plate was 2066 K. This temperature is about 4% higher than that predicted from the numerical calculation (1986 K).

### 4.2. Graphite Plate Erosion

Since the combustion of carbon occurs at the surface of the graphite plate, carbon is oxidized into $CO_2$. As a plume of hot air rises from the bottom of the plate, the boundary layers on the side walls are thinner at

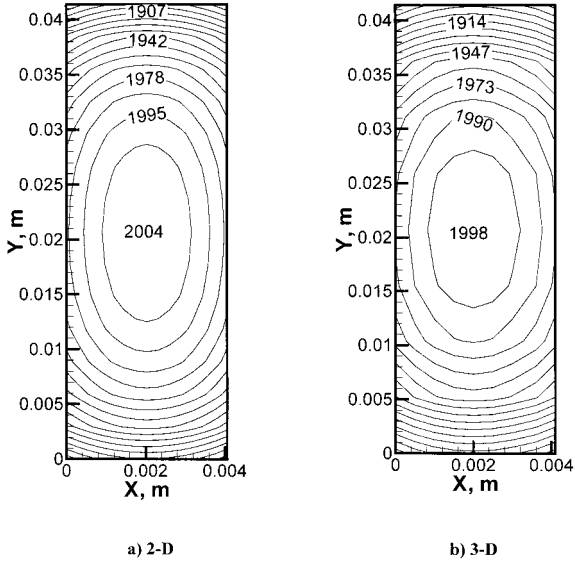


**Fig. 7.** Comparison of temperature distributions at the midplane of the graphite plate obtained from 2-D and 3-D analysis.

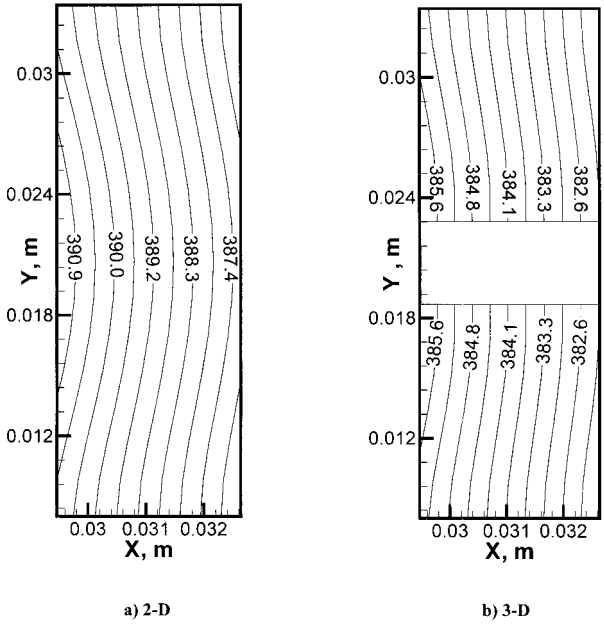


**Fig. 8.** Comparison of temperature distributions in the copper substrate obtained from 2-D and 3-D analysis.

the bottom than at the top. As a result, higher heat and mass transfer occur at the bottom and, in turn, the bottom of the plate erodes more than the top. The plate thickness also decreases with time. It was found that in 10 min, the top of the graphite plate eroded 0.7 mm, whereas the bottom eroded 2.5 mm. The entire height of the plate decreased from 4.14 cm to the

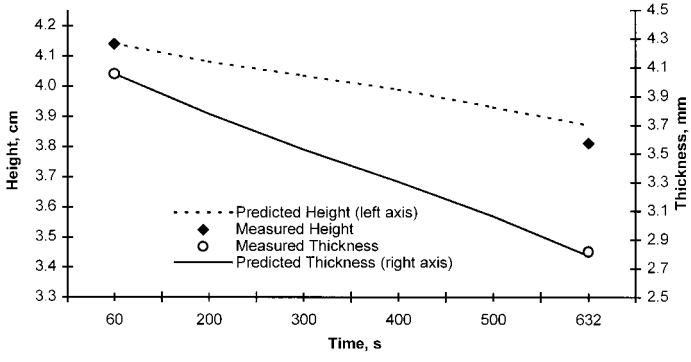


**Fig. 9.** Change in the graphite plate height and thickness.

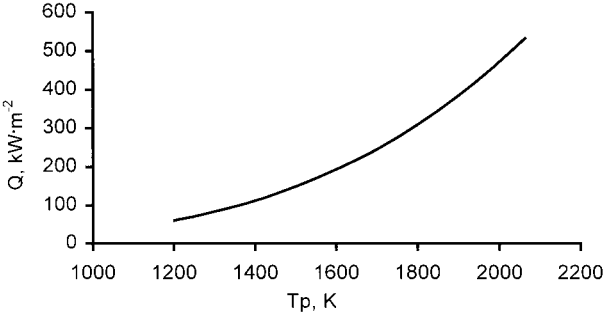


**Fig. 10.** Numerically calculated gauge heat flux vs graphite plate surface temperature.

final value of 3.81 cm. During this period, the initial thickness of the plate in the middle decreased from 0.41 to 0.28 cm. Both the experimental and the numerical results are shown in Fig. 9. The agreement between the measured and calculated height and the average thickness of the plate is acceptable.

### 4.3. Heat Flux Calibration

It can be noted from the foil gauge analysis that the temperature distribution in the foil gauge depends on the heat flux imposed on it from the graphite plate and the temperature of the copper substrate. The heat flux imposed by the graphite plate depends strongly on the temperature of the graphite plate. Figure 10 shows the heat flux on the foil gauge as a function of the graphite plate surface temperature, which was varied parametrically. The temperature distribution in the foil gauge corresponding to a graphite plate surface temperature of 1986 K and a copper substrate temperature of 384 K are shown in Fig. 11. It should be noted that because of the coupling,

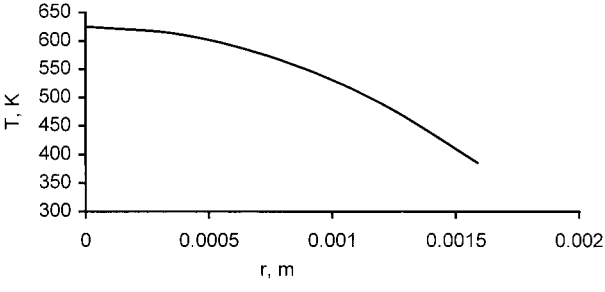


**Fig. 11.** Temperature distribution along the foil gauge.

although weak, between the temperature distribution in the foil gauge and the imposed heat flux, an iterative procedure was used to solve for the two simultaneously. The temperature difference between the center and the edge of the foil is usually determined from the output of the copper–constantan thermocouples, which are placed at the center and at the junction between the foil gauge and the copper support structure.

The gauge output in millivolts can be related to the imposed heat flux. The solid line in Fig. 12 shows the predicted heat flux on the foil surface as a function of the thermocouple output in millivolts. The dotted line in Fig. 12 represents the calibration curve provided by the manufacturer. The heat fluxes predicted from the model are lower than those obtained from the calibration curve. For example, for a thermocouple output of 10 mV, the predicted heat flux is $360\,\mathrm{kW \cdot m^{-2}}$, whereas the heat flux obtained from the calibration is $450\,\mathrm{kW \cdot m^{-2}}$. Similarly, for a heat flux of $470\,\mathrm{kW \cdot m^{-2}}$, the predicted thermocouple output is 13 mV, whereas the calibration curve gives an output of 10.8 mV.

Due to the oxidation of the graphite plate surface, the height and thickness of the graphite plate decrease with time. The resistance of the graphite plate increases because of the reduction in the cross-sectional area of the graphite plate. As the voltage remains constant, the power input to the graphite plate decreases. This leads to a decrease in the graphite plate temperature, and, in turn, the net radiative heat flux from the graphite plate reaching the gauge decreases with time. Given a nominal experimental condition for heat flux of $477\,\mathrm{kW \cdot m^{-2}}$, applied for 10 min, a comparison is made between the measured heat flux versus time and the numerically

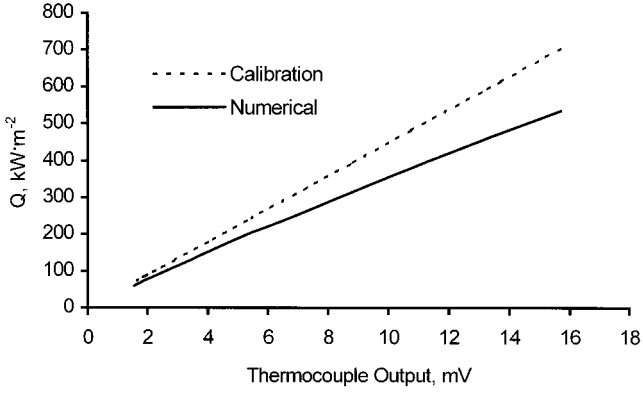


**Fig. 12.** Numerically calculated gauge heat flux vs foil gauge millivolt reading of the copper–constantan thermocouple.

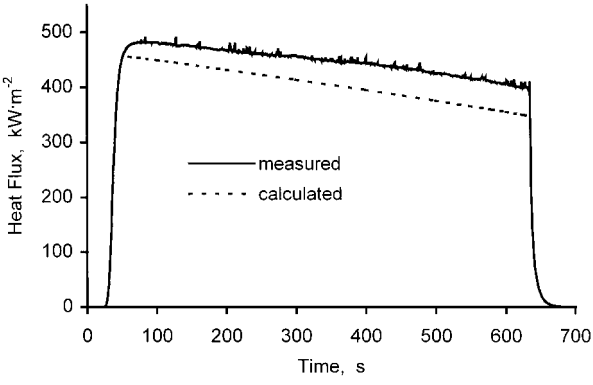


**Fig. 13.** Comparison of the experimental and numerically calculated gauge heat flux.

calculated heat flux versus time as shown in Fig. 13. The difference between the experimental and numerical prediction of heat flux is less than 5%.

### 4.4. Grid Sensitivity

The numerical model described in Section 3 was first tested for its accuracy by comparing the calculated gauge heat flux with the experimental data using the $7 \times 7$ mesh size. The error was $\sim 5\%$. For testing the grid resolution, the computations were performed by increasing the mesh density from $7 \times 7$ to $47 \times 47$. The numerical results are plotted in Fig. 14. From Fig. 14, it can be seen that as the number of mesh points increase, the heat flux increases and reaches an asymptotic value. As the difference between the $27 \times 27$ and the asymptotic heat flux values is approximately

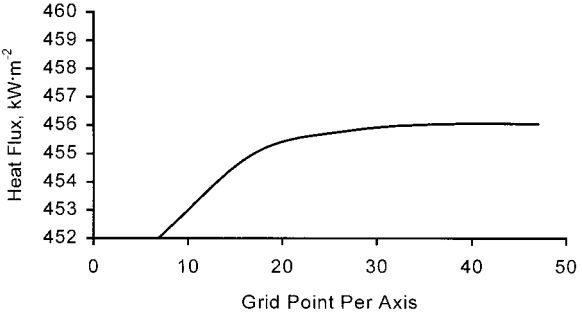


**Fig. 14.** Grid sensitivity.

1%, the computations in this study were performed with the $27 \times 27$ mesh to save computation time with sufficient accuracy of numerical result.

### 4.5. Possible Reasons for the Discrepancies Between Experimental Results and Numerical Computations

From the comparisons discussed in Sections 4.1, 4.2, and 4.3, several reasons for the differences between the numerical predictions and the experimental data are possible. These are discussed below.

#### *4.5.1. Experimental Error*

Various measurements made during the course of the experiment have uncertainties associated with them. Sources of these uncertainties include the readings of the voltmeter, the current meter, and the voltage transducers, as well as the electric current measurement coil and the optical pyrometer.

The uncertainty estimates for various measurements are summarized in Table I. The total uncertainty in a measurement is the square root of the sum of the squares of the component uncertainties. Uncertainties in the heat flux gauge calibration are not included since the objective of this work is to define those uncertainties.

Uncertainties in the graphite plate dimension measurements are as follows: $\pm 0.25$ mm for thickness and $\pm 0.1$ mm for height. The thickness uncertainty is relatively large due to the uneven nature of the graphite plate surfaces after erosion has occurred. A small, but unknown, amount of erosion occurs prior to the startup time used in the analysis. This erosion occurs during a short heating of the plate to verify proper clamping of the plate and during the transient startup of each experimental run.

**Table I.** Experimental Measurement Uncertainty[a]

| Source | Measurement | | | |
|---|---|---|---|---|
| | Heat flux | Plate current | Plate voltage | Plate temperature |
| Voltmeter | $\pm 1\ \mathrm{kW \cdot m^{-2}}$ | $\pm 0.4$ A | $\pm 0.009$ V | |
| Current transformer | | $\pm 24$ A | | |
| Current transducer | | $\pm 15$ A | | |
| Volt transducer | | | $\pm 0.225$ V | |
| Optical pyrometer | | | | $\pm 3$°C |
| Total uncertainty | $\pm 1\ \mathrm{kW \cdot m^{-2}}$ | $\pm 28.3$ A | $\pm 0.225$ V | $\pm 3$°C |

[a] All uncertainties are derived from the manufacturer's data.

*4.5.2. Uncertainty in the Parameters Used in the Numerical Model*

The values of the various parameters used in the numerical model were obtained from a variety of sources. The foil gauge is the most sensitive part in the thermal gauge; the foil diameter and thickness were obtained from the gauge manufacturer. Changing the thickness of the gauge by $\pm 10\%$ from its nominal value of 51 $\mu$m, the change in heat flux is $\pm 0.4\%$, while the millivolt output changes are $-7.7$ and $12.7\%$, respectively. Similarly, a $\pm 10\%$ change in the thermal conductivity of the foil affects the heat flux only by $\pm 0.8\%$, but the thermocouple output is changed by $-7.5$ and $+12.5\%$. The overprediction by the model, the thermocouple output (13 mV compared to the experiment) for a given heat flux ($456\ \mathrm{kW \cdot m^{-2}}$), can be explained mostly by the $\sim 10\%$ increase in the thermal conductivity and thickness of the foil. Overprediction can also occur if the diameter of the foil is smaller than the actual diameter used in the analysis. However, the uncertainty due to variations in the foil diameter was not calculated.

Material properties of the ATJ graphite were obtained from the material manufacturer. Properties for the copper substrate in the heat flux gauge were taken from a handbook. Emissivities of the graphite plate and black paint which coated the heat flux gauge face were obtained using an emissivity measuring optical pyrometer described by Cameron [5]. The emissivity of the graphite plate used in the numerical model is 0.97. Most properties were obtained as functions of temperature. However, some properties, such as the emissivity of the paint on the gauge face, could be obtained only for room temperature. The value used in the model is 0.95.

Errors are introduced into the numerical calculation since the manufacturer and handbook data represent typical values as opposed to measurements for the actual pieces of material used. Properties known only at room temperature are likely to vary somewhat with temperature, thereby introducing another error into the calculation.

Electrical current passing through the plate is the primary energy source in the model and was obtained from measurements. These measurements have an uncertainty associated with them. This uncertainty is another source of error in the numerically calculated heat flux.

There is uncertainty in the heat and mass transfer coefficients as well. But their effect on the end results is very small. When the heat transfer coefficient changes by $\pm 10\%$, the heat flux and the thermocouple output change by only $\pm 2\%$. A change of $\pm 10\%$ in the mass transfer coefficient leads to only $\pm 0.01\%$ uncertainty in the heat flux and the thermocouple output.

Table II summarizes the effect that variations in several parameters have on the numerical results.

**Table II.** Uncertainty in the Numerical Calculation of Heat Flux and Thermocouple Output at the Foil Gauge Due to Uncertainties in Various Parameters[a]

| Source | Numerical result | |
|---|---|---|
| | Heat flux | Thermocouple output |
| Emissivity of foil gauge | | |
| +0.05 | +5.1% | +6.8% |
| −0.05 | −5.1% | −4.2% |
| Current in the graphite plate | | |
| +24 A | +4% | +6.7% |
| −24 A | −4% | −3% |
| Thermal conductivity of foil | | |
| +10% | +0.8% | −7.5% |
| −10% | −0.8% | +12.5% |
| Foil gauge thickness | | |
| +10% | +0.4% | −7.7% |
| −10% | −0.4% | +12.5% |
| Heat transfer coefficient | | |
| +10% | −0.2% | −0.2% |
| −10% | +0.2% | +0.2% |
| Mass transfer coefficient | | |
| +10% | −0.01% | −0.01% |
| −10% | +0.01% | +0.01% |

[a] Nominal value of heat flux is $456\ \mathrm{kW \cdot m^{-2}}$. Nominal value of thermocouple output is 13 mV.

## 5. CONCLUSIONS

A pseudo-three-dimensional finite difference model of a flat plate heat flux gauge calibration system has been developed. The numerical solution provides the temperature distribution in the thickness of the flat plate heating element and the heat flux gauge, the heat flux at the gauge face, and the shape change of the flat plate with time. Comparison with data from experiments has also been performed. The difference between the experimentally measured (through the calibration curve) and the calculated heat flux is less than 5%. However, the model overpredicts the thermocouple output by about 17%. This discrepancy may be due to the uncertainty in the values of the various parameters used in the numerical model. The numerical analysis will eventually be extended to uncooled heat flux gauges operating at a high (850°C) temperature.

## NOMENCLATURE

| | |
|---|---|
| $A$ | Area |
| $B_h$ | Blowing parameter |
| $C_p$ | Specific heat |
| $D$ | Diameter of the heat flux gauge |
| $DI$ | Channel diameter |
| $D_{12}$ | Oxygen Diffusion coefficient |
| $F$ | Shape factor |
| $Gr$ | Grashof number |
| $g$ | Acceleration due to gravity |
| $H$ | Height |
| $\Delta H_c$ | Heat released per kilogram of carbon |
| $h_c$ | Average natural convection heat transfer coefficient |
| $I$ | Electrical current through the graphite plate |
| $k$ | Thermal conductivity |
| $L$ | Length |
| $Q'''$ | Heat generation per unit volume of the graphite plate |
| $q$ | Heat flux |
| $m_{1,e}$ | Oxygen mass concentration near the graphite plate surface |
| $m_{1,s}$ | Oxygen mass concentration in the ambient air |
| $\dot{m}''$ | Mass transfer rate from the horizontal graphite plate surface |
| $n_{1,s}$ | Oxygen mass flux near the graphite plate surface |
| $n_{2,s}$ | Carbon dioxide mass flux near the graphite plate surface |
| Pr | Prandtl number |
| $R$ | Electrical resistance |
| $r$ | Radial coordinate |
| Re | Reynold number |
| Sc | Schmidt number |
| $T$ | Temperature |
| $\Delta T$ | Temperature difference between the surface and the ambient |
| $TH$ | Thickness |
| $x$ | Horizontal coordinate |
| $x'$ | Shifted horizontal coordinate |
| $y$ | Vertical coordinate |
| $z$ | Horizontal coordinate |

### Greek Letters

| | |
|---|---|
| $\beta_{1m}$ | Mass transfer driving force |
| $\delta$ | Thickness of the foil |
| $\varepsilon$ | Radiation emissivity |

| | |
|---|---|
| $\eta$ | Mass transfer conductance |
| $\lambda$ | Specific resistance |
| $v$ | Kinematic viscosity |
| $\rho$ | Density of the graphite plate |
| $\sigma$ | Stefan–Boltzmann constant |
| $\varphi$ | Prandtl number function |

### Subscripts

| | |
|---|---|
| 1 | Oxygen |
| 2 | Carbon dioxide |
| c | Copper substrate |
| $D$ | Cylindrical surface |
| e | Environment (ambient) |
| f | Thermal foil gauge |
| h | Horizontal surface |
| p | Graphite plate |
| s | Surface |
| v | Vertical surface |
| water | Water-cooled |

### Superscripts

| | |
|---|---|
| 0 | Zero mass transfer |
| d | Heated plate facing down |
| u | Heated plate facing up |

## REFERENCES

1. D. Holmberg, K. Steckler, C. Womeldorf, and W. Grosshandler, in *Proceedings of the ASME International Mechanical Engineering Conference and Exhibition* (ASME, New York, 1997), Vol. 3, p. 165.
2. W. L. Grosshandler and D. Blackburn, in *Proceedings of the ASME International Mechanical Engineering Conference and Exhibition* (ASME, New York, 1997), Vol. 3, p. 153.
3. A. V. Murthy, B. K. Tsai, and R. D. Saunders, in *Proceedings of the ASME International Mechanical Engineering Conference and Exhibition* (ASME, New York, 1997), Vol. 3, p. 159.
4. T. J. Horn, *Comparison of Heat Flux Standard for Calibration Heat Flux Gage at Elevated Temperature and High Heat Flux Levels*, Master's thesis (Virginia Polytechnic Institute and State University, Blacksburg, 1993).
5. E. S. Cameron, *SPIE* **1044**:155 (1989).
6. A. F. Mills, *Basic Heat and Mass Transfer* (Prentice–Hall, Upper Saddle River, NJ, 1999).
7. S. V. Patankar, *Numerical Heat Transfer and Fluid Flow* (Hemisphere, New York, 1984).